Supplemental Materials for "High quality-factor space-time metasurface for free space power isolation at near-infrared regime"

Raana Sabri and Hossein Mosallaei[1, a)]

Department of Electrical and Computer Engineering, Northeastern University, Boston, MA, 02115, USA

(Dated: 8 December 2023)

The Supplemental Material is organized in eight sections:

S1. Validation of RSTWA Simulations with COMSOL Multiphysics

S2. Investigation of Optical Spectrum of DBR

S3. Optical Response of the Unitcell under Oblique Illumination of Incident Light

S4. Quality-factor Calculation of the Resonant Modes

S5. Physical Explanation of the High-Q Mode by Multipole Decomposition

S6. Radiation Efficiency

S7. Device Simulations and Carrier Dynamics

S8. Waveform Optimization

[a)]Electronic mail: hosseinm@ece.neu.edu

S1. VALIDATION OF RSTWA SIMULATIONS WITH COMSOL MULTIPHYSICS

The optical simulations of our proposed all-dielectric high-Q metasurface, presented in the main manuscript, is carried out by our in-house developed RSTWA [72]. As discussed in the main manuscript, RSTWA provides a scattering matrix relationship between the incident and scattered fields of the structure at its spatiotemporal harmonics by enforcing the boundary conditions and taking the periodic spatiotemporal profile of the permittivity into the Fourier domain. We have employed the commercial software COMSOL Multiphysics for validating the RSTWA results at the absence of time-modulation. The software allows for fast and accurate analysis of the structure by providing a two-dimensional solution space in the account for infinitely long metasurface along the y-direction and adaptive meshing to guarantee the convergence of the optical results. The unit cell is modeled in the 2D space dimension and periodic boundary condition is selected along the x-axis. The plane wave "Periodic" port is used for metasurface excitation, where the wave is propagating along the z-axis. The scattering condition is enforced along the z-direction in order to absorb the light and eliminate its back and force propagation. Figure S1 illustrates the reflection amplitude and phase of the proposed unit cell in the absence of time-varying RF bias voltage, where the structural parameters are set as revealed in the main manuscript. A great agreement can be observed between the results generated by RSTWA and COMSOL. In addition, the near field profile of the unit cell is calculated by COMSOL and illustrated in Fig. S1(c) that demonstrates the characteristics of the magnetic octupole as discussed in the main manuscript.

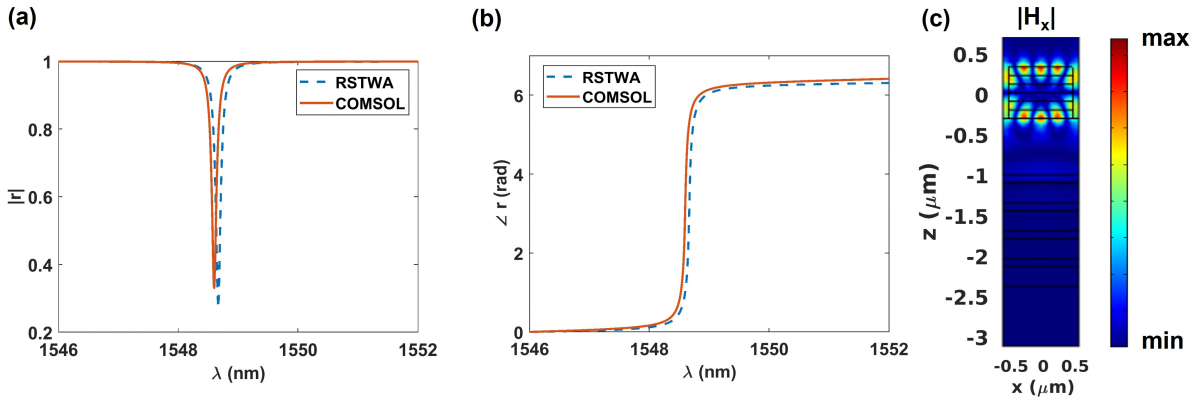

Fig. S 1. Reflection (a) amplitude and (b) phase of the proposed high-Q all-dielectric unit cell, under normal illumination of the TE-polarized light. Blue dashed lines represent RSTWA results while red solid lines demonstrate the COMSOL data. There is a great agreement between the results. (c) The near-field depiction of the x component of the magnetic field within the metasurface unit cell obtained by COMSOL, that shows magnetic octupole mode.

S2. INVESTIGATION OF OPTICAL SPECTRUM OF DBR

Although increasing the number of DBR pairs that is used as a backmirror in our proposed metasurface configuration leads to higher levels of reflection, it makes the metasurface bulky and heavy which is not desired. It is crucial to obtain higher levels of reflection while keeping the metasurface as compact as possible. In this section, we have studied the optical reflection spectra of the DBR configuration consisting of 2, 4, 6, and 8 pairs of Si/SiO_2 layers and compared the results against the lossless SWG on top of the 4 layer DBR. The thickness of each DBR layer is adjusted to $\lambda_0/4n_{\text{eff}}$, where λ_0 is the wavelength of incident light and n_{eff} is the refractive index of consisting materials. The simulation is performed by COMSOL Multiphysics where the boundary conditions along the x and y directions are set as periodic and PML is assigned to the top and bottom boundaries. From the results shown in Fig. S2, one can see that under the illumination of TE polarized plane wave, the reflectivity is increased from 0.955 to 0.998 by adding only two layers of Si/SiO_2 DBR. Further increment of the DBR pairs to six and eight results in only a negligible improvement of the reflection coefficient (< 0.0005) as it is observed in the inset of Fig. S2. Therefore, we have fixed the number of DBR pairs at four since it offers relatively high reflection response and keeps the thickness of the entire metasurface compact.

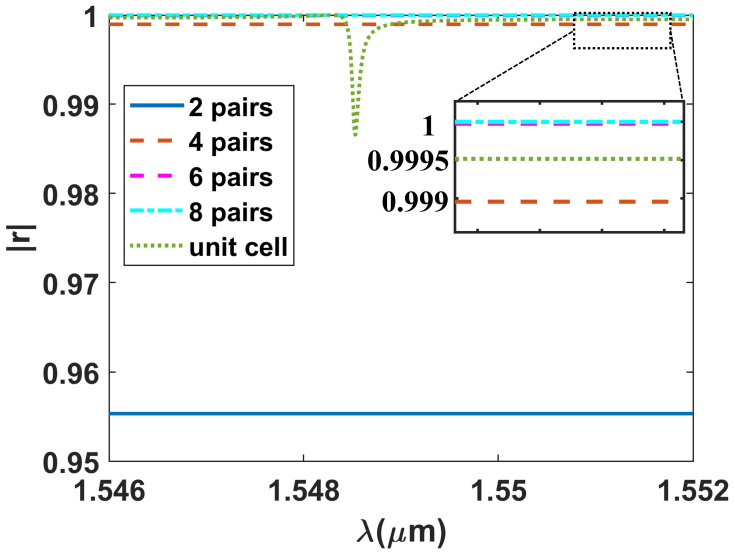

Fig. S2. Reflection spectra of the DBR layers consisting of 2, 4, 6, and 8 layers. The close-up shows the magnified reflection amplitude at the range 0.9985 to 1.

S3. OPTICAL RESPONSE OF THE UNITCELL UNDER OBLIQUE ILLUMINATION OF INCIDENT LIGHT

In this section, we have studied the sensitivity of the metasurface optical response into the incident angle that varies in the range of $0^\circ - 10^\circ$. As it can be observed from the results in Fig. S3 that are generated by COMSOL, the optical mode is angle-sensitive and is shifted toward the shorter wavelengths by increasing the incident angle up to 10°. In addition, it is clear that for 1° deviation of the incident angle, the resonant mode experiences a different spectral shift at smaller and steeper angles. In particular, when the incident angle increases from 0° to 1°, the spectral shift of the resonance is ≈ 0.3 nm, while it is around ≈ 4 nm for the incident angle changing from 9° to 10°. This is due to the impedance mismatch between the incident and reflected light by moving toward the steeper angles. It is worth mentioning that the spectral shift of the resonant mode is ≈ 25 nm when the incident light grows steeper from normal direction to 10°. This is while for the same level of the incident angle variation, the nonlocalized beams such as guided mode resonances experience an spectral shift at the order of 150 nm as it is evident in [35].

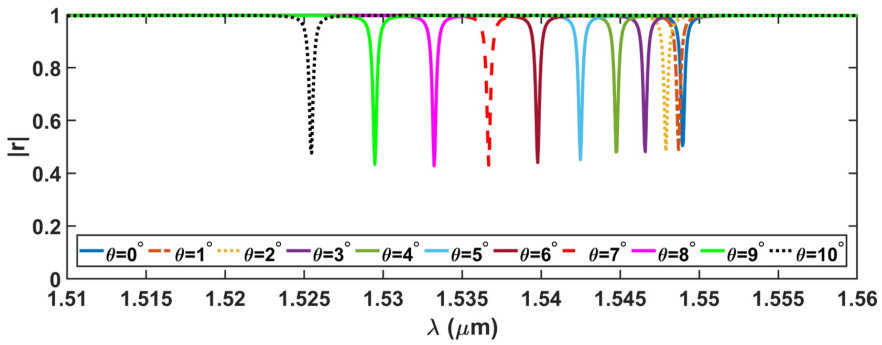

Fig. S3. Reflection amplitude of the metasurface unit cell under the illumination of oblique light, whose incident angle increases form 0° to 10°.

S4. QUALITY-FACTOR CALCULATION OF THE RESONANT MODES

In section 2 of the main manuscript, we have demonstrated the capability of our proposed all-dielectric metasurface in supporting two anti-crossing resonant modes by changing the dimension of the SWG. As it is discussed, the resonant modes demarcated by the red and black circles, respectively are associated with the low- and high-Q resonances. In this section, we have calculated the Q-factor of the resonances that is defined as the ratio of the resonance frequency to the half power bandwidth of the resonator ($Q = f_0/\Delta f$) for the two branches showed in Figs. 2(a)-(b) of the main manuscript. By choosing different values for the height and width of the SWG, we can observe the anti-crossing of the optical modes. For the optimal geometrical parameters of the SWG, the high Q-factor is achieved along the black branch that corresponds to magnetic octupole and its Q-factor is calculated as 11876. Figures S4(a)-(b) show the Q-factor of the resonant modes when w is increasing from 600 nm to 900 nm with 10 nm steps, where h_1 is fixed at 684 nm, as well as the case when h_1 is varying in the range of 400-700 nm with 10 nm resolution, while w is adjusted to 853 nm, respectively. As it can be seen, the Q-factors of the mode depicted by the red markers are at the order of ≈ 1000 and always remain below the black branch, while the largest value reaches up to ≈ 2000 at $w = 690$ nm. At the anti-crossing point, when the spectral splitting between the modes takes place (as depicted in Fig. 2(a) of the main manuscript), the Q-factor on the red branch shows a clear minimum at around 700 nm, while the mode on the black branch achieves the maximal Q-factor of ≈ 11778. By moving away from the anti-crossing point, the Q-factors of the mode at the black branch drop significantly giving rise to power radiation out of the resonator. For the values of w beyond 740 nm, the low-Q mode on the red branch maintains

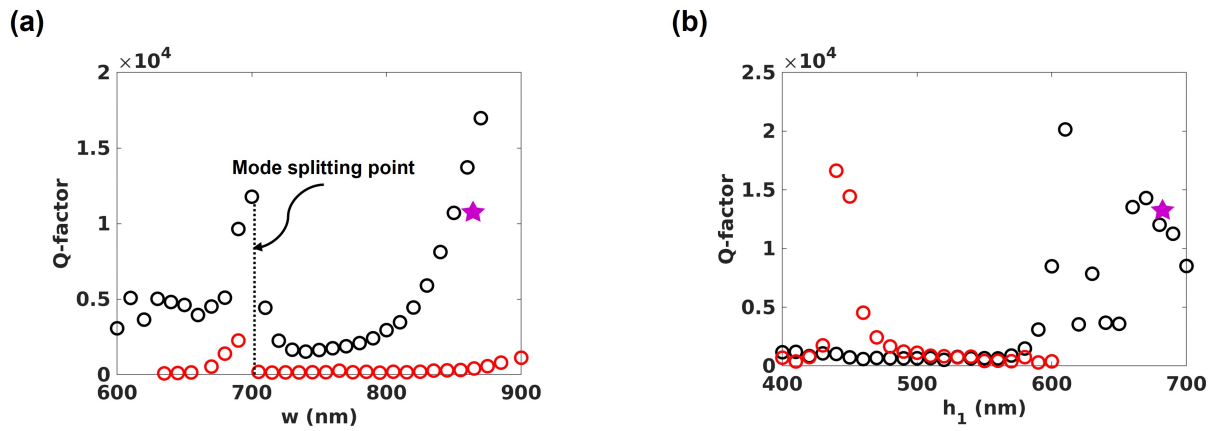

Fig. S4. Q-factor calculation for the two anti-crossing resonant modes supported by the metasurface unit cell as functions of SWG (a) width (w) and (b) height h_1. The dashed line in (a) shows the anti-crossing (mode splitting) point. The magenta pentagonal marker depicts the width and height corresponding to the supported magnetic octupole resonant mode at 1.55 μm

an almost constant Q-factor. Nevertheless, the Q-factor of the other mode on the black branch gradually increases by increasing the resonator width and it reaches to the maximal Q-factor of ≈ 16978 at $w = 870$ nm. On the other hand, as illustrated in Fig. S4 (b), both the resonant modes depict the high Q-factor at the specific values of the resonator height namely 440 nm and 610 nm on the red and black branches, respectively. The largest Q-factor is calculated as ≈ 20150 for the mode demonstrated by the black trajectory. The Q-factors of the mode on red branch have not been calculated for h_1 beyond 600 nm, as the spectral shift of the resonant mode moves it out of our interested regime. Unlike the previous case, here around the anti-crossing point, both the resonant modes demonstrate relatively low Q-factor. The resonant mode on the black branch maintains larger Q-factors for $h_1 > 580$ nm that surpasses that of the resonant mode demarcated by red circles. To conclude, we observed that by keeping the height of the SWG constant and varying its width, ultrahigh Q-factors can be maintained on one of the resonant modes represented by black circles that is called as high-Q mode. however, significantly large Q-factors can be yielded by both resonant modes that are depicted by black and red circles, when the height of SWG is fixed while we alter its width.

S5. PHYSICAL EXPLANATION OF THE HIGH-Q MODE BY MULTIPOLE DECOMPOSITION

To provide a better insight into the radiative properties of the high-Q metasurface and figure out the origin of the supported mode., we employed the multipole decomposition of the metasurface scattering response. In this section, we use the discussion in [89, 90] to provide the detailed formulation toward developing multipole representations of the scattering coefficient. For an arbitrarily-shaped particles under the illumination of time-dependent monochromatic electric field of $\exp(-i\omega t)$, the induced multipole moments by the incident light can be determined by the polarization vector $\mathbf{P}(\mathbf{r}') = \varepsilon_0(\varepsilon_\mathrm{p} - \varepsilon_\mathrm{d})\mathbf{E}(\mathbf{r}')$, wherein ε_0, ε_p, ε_d are the dielectric permittivities of the free space, particle, and surrounding medium, respectively, while $\mathbf{E}(\mathbf{r}')$ represents the total electric field inside the scatterer and $\mathbf{r}'$ is the radius position vector of the observation point. The induced electric current density can be then described as $\mathbf{j}(\mathbf{r}') = -i\omega\mathbf{P}(\mathbf{r}')$. By assuming that the origin of the Cartesian coordinate system is located at the center of scatterer, multipole moments up to the third order can be written as [79]:

$$\mathbf{p}_0 = \frac{i}{\omega}\int_{V_\mathrm{s}} j_0(k_\mathrm{d} r')\mathbf{j}(\mathbf{r}')d\mathbf{r}' \tag{S1}$$

$$\mathbf{m}_1 = \frac{3}{2}\int_{V_\mathrm{s}} \frac{j_1(k_\mathrm{d} r')}{k_\mathrm{d} r'}[\mathbf{r}'\times\mathbf{j}]d\mathbf{r}' \tag{S2}$$

$$\hat{Q}_1 = \frac{3i}{\omega}\int_{V_\mathrm{s}} \frac{j_1(k_\mathrm{d} r')}{k_\mathrm{d} r'}[3(\mathbf{r}'\mathbf{j}+\mathbf{j}\mathbf{r}') - 2(\mathbf{r}'.\mathbf{j})\hat{U}]d\mathbf{r}' \tag{S3}$$

$$\hat{M}_2 = 5\int_{V_\mathrm{s}} \frac{j_2(k_\mathrm{d} r')}{(k_\mathrm{d} r')^2}([\mathbf{r}'\times\mathbf{j}]\mathbf{r}' + \mathbf{r}'[\mathbf{r}'\times\mathbf{j}])d\mathbf{r}' \tag{S4}$$

$$\mathbf{T}_2 = \frac{ik_\mathrm{d}{}^2}{\omega^2}\int_{V_\mathrm{s}} \frac{j_2(k_\mathrm{d} r')}{(k_\mathrm{d} r')^2}[3(\mathbf{r}'.\mathbf{j})\mathbf{r}' - r'^2\mathbf{j}]d\mathbf{r}' \tag{S5}$$

$$\hat{O}_2{}^{(\mathrm{e})} = \frac{15i}{\omega}\int_{V_\mathrm{s}} \frac{j_2(k_\mathrm{d} r')}{(k_\mathrm{d} r')^2}(\mathbf{j}\mathbf{r}'\mathbf{r}' + \mathbf{r}'\mathbf{j}\mathbf{r}' + \mathbf{r}'\mathbf{r}'\mathbf{j} - \hat{A})d\mathbf{r}' \tag{S6}$$

$$\hat{Q}_3 = \frac{6ik_\mathrm{d}{}^2}{\omega}\int_{V_\mathrm{s}} \frac{j_3(k_\mathrm{d} r')}{(k_\mathrm{d} r')^3}[5(\mathbf{j}.\mathbf{r}')\mathbf{r}'\mathbf{r}' - r'^2(\mathbf{j}\mathbf{r}'+\mathbf{r}'\mathbf{j}) - (\mathbf{j}.\mathbf{r}')r'^2\hat{U}]d\mathbf{r}' \tag{S7}$$

$$\hat{O}_3{}^{(\mathrm{m})} = \frac{105}{4}\int_{V_\mathrm{s}} \frac{j_3(k_\mathrm{d} r')}{(k_\mathrm{d} r')^3}([\mathbf{r}'\times\mathbf{j}]\mathbf{r}'\mathbf{r}' + \mathbf{r}'[\mathbf{r}'\times\mathbf{j}]\mathbf{r}' + \mathbf{r}'\mathbf{r}'[\mathbf{r}'\times\mathbf{j}] - \hat{A}')d\mathbf{r}' \tag{S8}$$

wherein k_{d} is the wave number in the surrounding medium, j_{l} is the lth order spherical Bessel function, $\hat{U}$ is the 3×3 unit tensor, and V_{s} is the volume of the scatterer.

The tensors $\hat{A}$ and $\hat{A}'$ can be represented as

$$A_{\beta\gamma\tau} = \delta_{\beta\gamma}V_{\tau} + \delta_{\beta\tau}V_{\gamma} + \delta_{\gamma\tau}V_{\beta} \tag{S9}$$

$$A'_{\beta\gamma\tau} = \delta_{\beta\gamma}V'_{\tau} + \delta_{\beta\tau}V'_{\gamma} + \delta_{\gamma\tau}V'_{\beta} \tag{S10}$$

in which $\beta = x,y,z$, $\gamma = x,y,z$, $\tau = x,y,z$, and $\delta_{\beta\gamma}$ is the Kronecker delta function, while V and V' can be described as

$$V = \frac{1}{5}[2(\mathbf{r}'.\mathbf{j})\mathbf{r}' + r'^2\mathbf{j}] \tag{S11}$$

$$V' = \frac{1}{5}r'^2[\mathbf{r}' \times \mathbf{j}]. \tag{S12}$$

After calculating the equations S1-S8 to obtain the exact contribution of multipole moments (the electric dipole $\mathbf{p}$, toroidal dipole $\mathbf{T}$, magnetic dipole $\mathbf{m}$, electric quadrupole tensor $\hat{Q}$, magnetic quadrupole tensor $\hat{M}$, electric octupole tensor $\hat{O}^{\mathrm{e}}$, and magnetic octupole tensor $\hat{O}^{\mathrm{m}}$), the total scattered power from the particle can be written as

$$P_{\mathrm{sca}} \approx \frac{k_0^4}{12\pi\varepsilon_0{}^2 v_{\mathrm{d}}\mu_0}|\mathbf{p}_0 + \mathbf{T}_2|^2 + \frac{k_0^4\varepsilon_{\mathrm{d}}}{12\pi\varepsilon_0 v_{\mathrm{d}}}|\mathbf{m}|^2 + \frac{k_0^6\varepsilon_{\mathrm{d}}}{1440\pi\varepsilon_0{}^2 v_{\mathrm{d}}\mu_0}\sum_{\alpha\beta}|Q_{1\alpha\beta} + Q_{3\alpha\beta}|^2 \tag{S13}$$
$$+\frac{k_0^6\varepsilon_{\mathrm{d}}{}^2}{160\pi\varepsilon_0 v_{\mathrm{d}}}\sum_{\alpha\beta}|M_{2\alpha\beta}|^2 + \frac{k_0^8\varepsilon_{\mathrm{d}}{}^2}{3780\pi\varepsilon_0{}^2 v_{\mathrm{d}}\mu_0}\sum_{\alpha\beta\gamma}|O^{(\mathrm{e})}{}_{2\alpha\beta\gamma}|^2 + \frac{k_0^8\varepsilon_{\mathrm{d}}{}^3}{3780\pi\varepsilon_0 v_{\mathrm{d}}}\sum_{\alpha\beta\gamma}|O^{(\mathrm{m})}{}_{3\alpha\beta\gamma}|^2$$

with v_{d}, k_0, and μ_0 being the speed of light in the surrounding medium, the wave number and permeability in the free space, respectively.

Once the exact multipole expressions are obtained, we use COMSOL multiphysics to calculate the contribution of each multipole in the output scattering response of the proposed all-dielectric unit cell, as depicted in Fig. 2(d) of the main manuscript. Nevertheless, due to the high Q-factors of the higher-order multipoles, they show smaller radiative properties compared to their lower-order counterparts. Therefore, in order to obtain a fair comparison and identify the nature of the supported mode, we have normalized the multiple moments such that they are in the same unit order. The normalized results are shown in Fig. S5. It is clear that at the operating wavelength of 1550 nm, the magnitude of the magnetic octupole moment is largest that defines the nature of the supported mode.

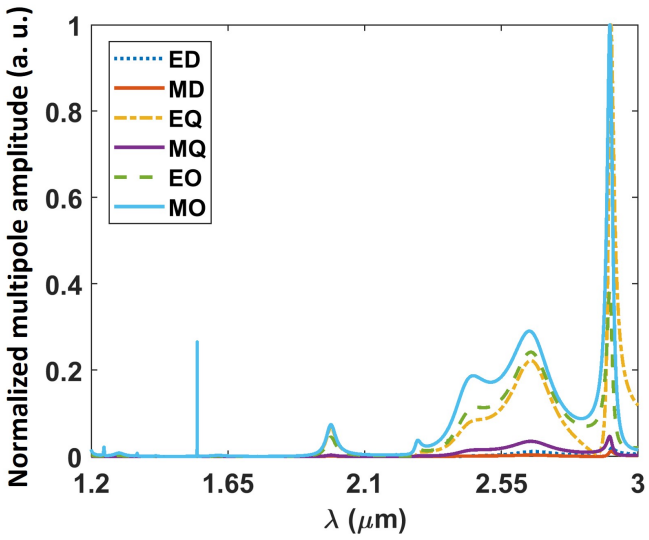

Fig. S5. The amplitude of the electric and magnetic multipoles up to the third order that are normalized to be in the identical metric. The dominant mode at the 1.55 μm corresponds to the magnetic octupole that describes the nature of supported mode.

S6. RADIATION EFFICIENCY

In this section, we have studied the radiation characteristics of our proposed high-Q metasurface. The radiation efficiency is a measure of directional capabilities of the metasurface that can be defined as the ratio of the radiated power into the incident power. For calculating the radiation performance of our metasurface, we have considered the outgoing power from the free standing SWG (without the buffer and DBR) enclosed by a surface. The power is then calculated by integrating the outgoing Poynting vector from the closed surface. To provide an insight, we calculated the radiation of the SWG at the wavelength 1548 nm corresponding to the high-Q magnetic octupole resonance and compared the results against the lower-order mode supported at the wavelength 2904 nm, which is characterized as electric dipole mode through conducting the multipole decomposition as shown in Fig. 2(d) of the main manuscript. From the results shown in Fig. S6 one can see that the radiated power from the electric dipole mode is $\approx 20\%$ larger than the magnetic octupole mode. The underlying reason is that the field is strongly confined within the resonator at magnetic octupole mode which is the reason for its ultrahigh Q-factor. The near-zone distributions of the magnetic and electric fields are also demonstrated at Figs. S6(b)-(c) at $\lambda = 2904$ nm and (d)-(e) at $\lambda = 1548$ nm, that confirm the origin of the resonances as electric

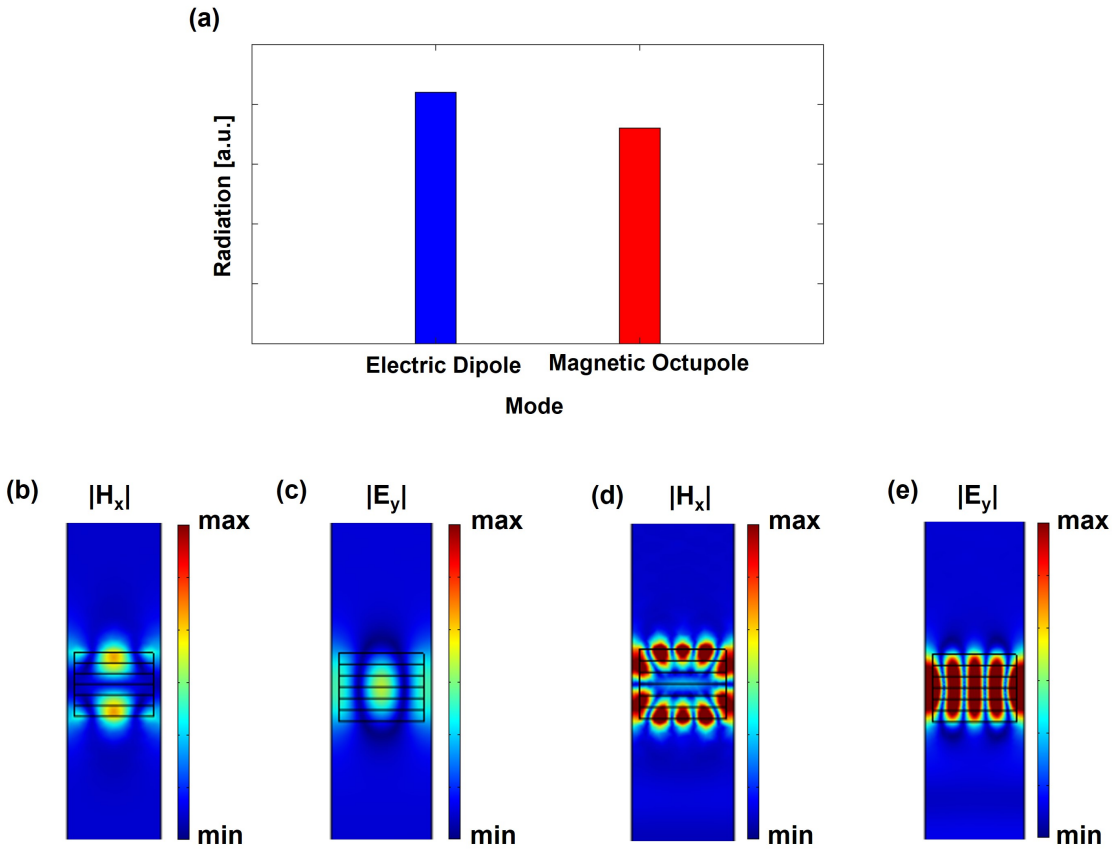

Fig. S6. (a) The radiation efficiency of free standing SWG at two operating modes. (b) The electric field and (c) magnetic field of the electric dipole resonant mode supported by the SWG at the operating wavelength of $\lambda = 2904$ nm and (d)-(e) same for the magnetic octupole at the $\lambda = 1548$ nm. The efficiency of the magnetic octupole mode is smaller due to confined electric field within the resonator that gives rise to Q-factor of resonance. The color bars are rescaled to be at the same range for the electric fields and magnetic fields of both modes to provide a fair comparison.

dipole and magnetic octupole, respectively. We also calculated the Q-factor for the electric dipole and magnetic octupoles supported by free standing SWG as ≈ 52 and ≈ 688, respectively that confirms the tradeoff between the Q-factor and radiation efficiency. It is worth mentioning that unlike the ultrahigh-Q magnetic octupole mode, the electric dipole mode with Q-factor of 52 cannot be dynamically modulated by the subtle change of the refractive index afforded by modulation mechanism in multijunction p-n layers.

S7. DEVICE SIMULATIONS AND CARRIER DYNAMICS

The carrier dynamic simulation of our proposed high-Q all-dielectric metasurface is carried out by using Lumerical device solver [91]. In the device simulations, the spatial distributions of the charge carriers are modeled under the application of the bias voltages through the Poisson and drift-diffusion equations. The carriers (electrons and holes) move under the influence of drift due to the applied bias voltages and random thermal diffusion due to the gradient in the density [7]. Silicon is modeled as a semiconductor, with the DC permittivity of $\varepsilon_{\rm dc} = 11.7$, the bandgap energy of $E_{\rm eg} = 1.115$ eV, the intrinsic work function of $W = 4.2$ eV, and the effective masses of electrons and holes of ${m_{\rm e}}^* = 1.18m_0$ and ${m_{\rm h}}^* = 1.18m_0$, respectively, with m_0 being the free electron rest mass. The aluminum with the work function of $W = 4.28$ eV is used as the contact pad for biasing the p-n multilayer configuration. The multijunction is biased by grounding the n-type regions and applying the respective bias voltage to the p-type regions that are electrically connected to each other. Therefore, a single set of voltage is required for biasing each unit cell. In the main manuscript, we remarked that the lower and upper boundaries of the bias voltages are adjusted to ensure the uniform carrier distribution within the p-n multijunctions. Figures S7(a)-(b) illustrate the spatial distributions of the holes and electrons within the p- and n-type regions as functions of the applied bias voltage which is changing from -1.2 to 1.5 V. At the unbiased case ($V = 0$ V), a narrow depletion zone is formed at the interfaces of the p-n junctions, which is due to the diffusion of the carriers to the regions with the major carrier distributions of the opposite charge. For the negative bias voltages ($V < 0$) and in the reverse bias mode, the p-type regions become more negative compared to the n-type regions and therefore, the thickness of the depletion layers is further increased. This is while, upon applying the positive bias voltage and switching to the forward bias mode, the thickness of the depletion layers shrinks and by further increasing the level of the bias voltage the charge carriers accumulate within the p-n layers. To provide a better insight on the uniformity of the carrier distribution within the p-n layers, we have plotted the spatial distributions of the holes and electrons for different bias voltages as depicted in Figs. S7(c)-(d). It is obvious that the distributions of the carrier densities are almost uniform for the voltages $V > 0.95$ with abrupt transitions that take place at the interfaces. On the other hand, increasing the bias voltage beyond 1.25 V or reducing it below < 0.95 V result in nonuniform distribution of the carriers even within the p-n layers and away from the interfaces as it is clear form the blue, red, yellow, and light blue curves. The change in the bias voltage from 0.95 V up to

1.25 V, enables accumulation of electrons and holes up to $N = 2.9 \times 10^{18}$ cm^{-3} and $P = 1.9 \times 10^{18}$ cm^{-3} in the n-type regions and $P = 2.9 \times 10^{18}$ and $N = 1.9 \times 10^{18}$ cm^{-3} in the p-type regions. The variations of the carrier densities within the p-n junctions for the allowed bias voltages is sufficient to modulate the refractive index of Si SWG to render the non-reciprocal response.

It should be noted that in order to accurately model the abrupt transitions at the interfaces of the p-n junctions, we have discretized the data in the distance 25 nm away from either sides of the p-n junctions into 5 homogeneous layers wherein the permittivity is considered uniform across the homogeneous discretized layers. The rest of the doped regions away from the interfaces is modeled with the homogeneous layer. Therefore, the entire p-n multijunction is divided into 56 sublayers along the z-direction with different permittivities that have been proved to be sufficient to ensure the converged results.

S8. WAVEFORM OPTIMIZATION

In the main manuscript, we have shown the ability of the high-Q space-time metasurface in generating highly asymmetric output spectrum in the non-adiabatic modulation regime and under time-reversal, that increases the isolation level between the fundamental frequency and the desired sidebands. In this section we have shown that we can further increase the isolation level between different ports of the isolator by optimizing the modulation waveform. For this purpose, we link the RSTWA to the genetic algorithm (GA) that is developed on the global optimization toolbox of MATLAB. The key metric is the reflection efficiency of the desired sideband. Therefore, the objective fitness function is defined as the reflection intensity at the desired sidabend to the summation of the reflected power at all sidebands, which can be expressed in the form of

$$\underset{P}{\text{maximize}} |r^{+1}|^2 / \Sigma_n |r^n|^2 \tag{S14}$$

where P is the vector defining the input parameter space. The input parameter space consists of 1×16 vector, whose elements correspond to the coefficients of the Fourier series which describes the profile of the modulation waveform. The lower and upper bounds of the parameter space are defined such that the modulation waveform does not surpass the allowed voltages that keep the refractive index uniform across the p-n multijunctions. Due to the relatively large number of the input parameters (1×16 matrix containing the Fourier series coefficients of the modulation waveform) the population size is adjusted to 200. The other options including the creation, crossover,

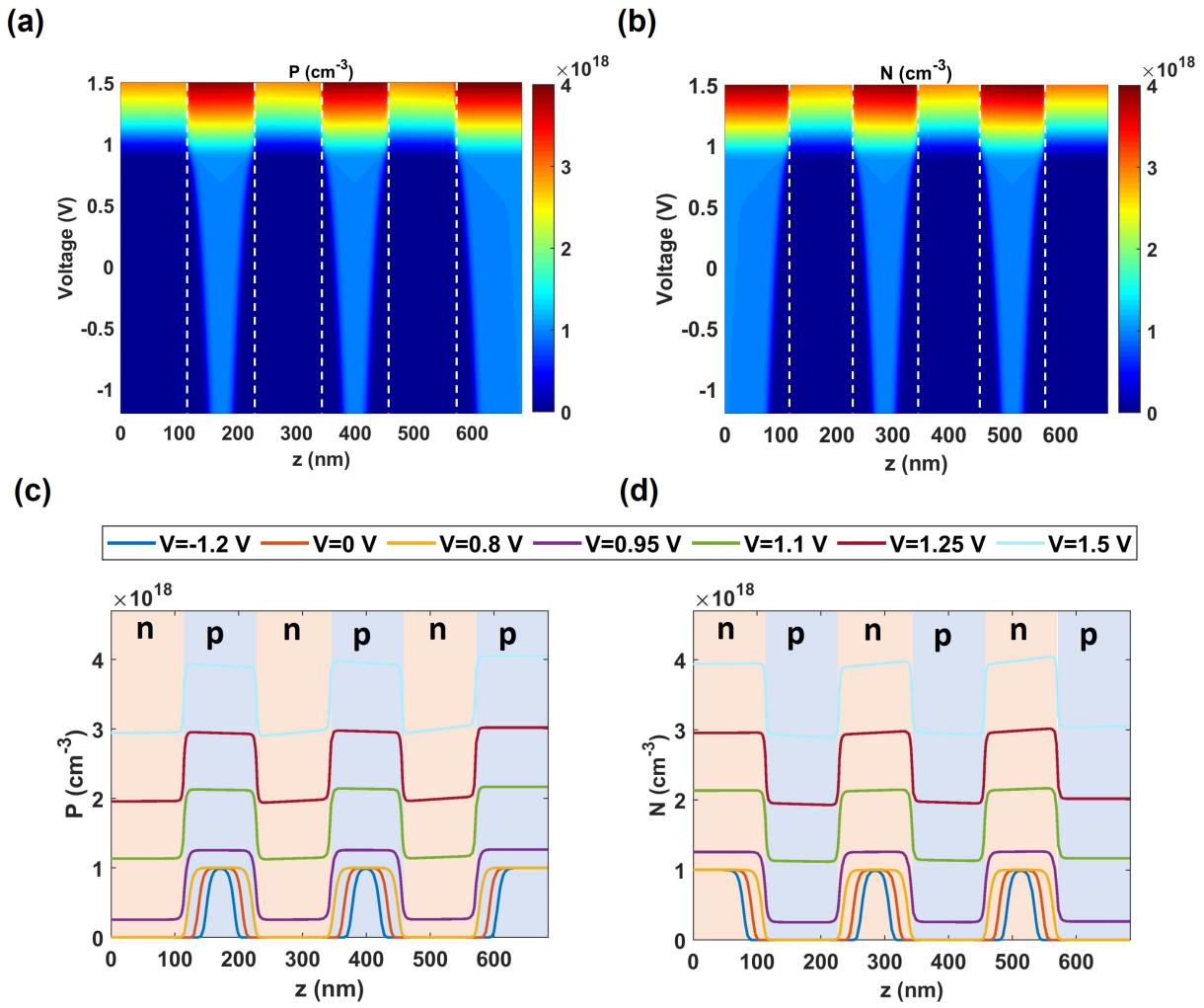

Fig. S 7. The spatial distributions of the (a) holes and (b) electrons within the p-n multijuction in the electrostatic mode as functions of the applied bias voltage. The 1D demonstrations of the (c) hole and (d) electron carriers for typical values of the applied bias voltages. For the bias voltages larger than the threshold level of $V_{\mathrm{T}} > 0.95$ V and smaller than 1.25 V, the carrier distribution is uniform across the n-type and p-type regions along the vertical direction. Outside this voltage range, the carrier distributions become nonuniform.

and mutation functions are set to the defaults of the global optimization toolbox of MATLAB R2019a. Figure S8 shows the normalized output spectrum of the high-Q all-dielectric metasurface whose waveform is optimized to maximize the throughput at the first-order up-modulated sideband. It can be seen that the normalized reflection is improved more than 1 dB (around 58% increase) compared to the case when sinusoidal modulation waveform is employed. The optimization is terminated when the improvement of the objective function is negligible by further

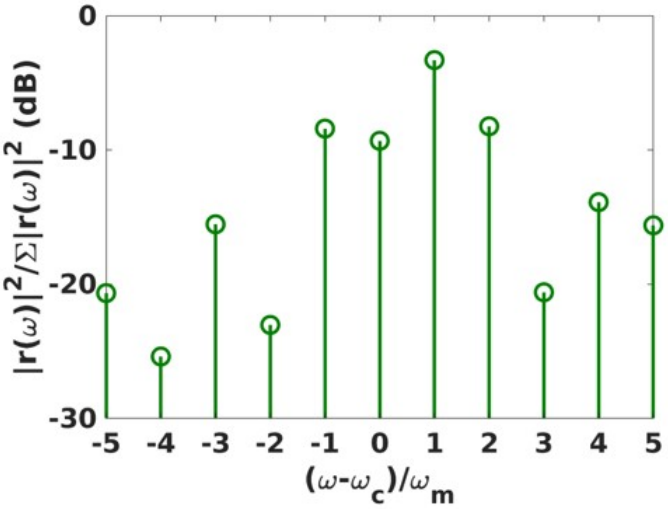

Fig. S 8. The normalized output spectrum of the space-time high-Q all-dielectric metasurface for the optimized modulation waveform for increasing the power at the desired first-order up-modulated sideband that shows 58% increase compared to the case excited by sinusoidal modulation waveform.

evolution of the proceeding generations.